CrossMark

Investigations of doping induced structural, optical and magnetic properties of Ni doped ZnS diluted magnetic semiconductors

D. Saikia[1] · J. P. Borah[1]

Abstract We have synthesized diluted magnetic semiconducting nanoparticles of undoped and Ni doped ZnS, by varying Ni concentration, via chemical co-precipitation technique. The formation of cubic zinc blend structure and the incorporation of Ni into ZnS lattice are confirmed by the X-ray diffraction (XRD) measurements. Rietveld refinement of the structural parameters shows a reasonable GOF value. Transmission electron microscopy result reveals the crystalline nature of the ZnS nanocrystal with an average d-spacing of 3.1 Å and also clarifies that the average particle size of the nanoparticles is in the range of 3–7 nm, which are consistence with the XRD results. UV–visible measurement depicts that the band gap of the Ni doped ZnS nanoparticles is higher than that of bulk ZnS, which is a result of the quantum confinement effect. Room temperature photoluminescence (PL) spectra shows the green emission in Ni doped ZnS nanoparticles, which is the characteristic $^3T_2$–$^3A_2$ transition of Ni^{2+} ion and also depicts the PL quenching effect at higher Ni concentration. Fourier transform infrared measurements show different stretching and vibrational modes and also show the resonance interactions of the sulphide ions. Raman analysis reveals different phonon modes of ZnS and confirms the defect states. Room temperature magnetic measurements demonstrate the ferromagnetic behavior in undoped ZnS nanoparticles due to the presence of structural defects. Systemic studies on the magnetic properties revels that all the doped ZnS nanoparticles exhibit the carrier mediated ferromagnetism and the saturation magnetization increases with increasing concentration of Ni.

1 Introduction

In recent years, diluted magnetic semiconductors (DMS) have attracted increasing attention in research due to their potential applications in nano-spintronics devices [1, 2]. Transition metal doped II–VI DMS have been mostly investigated among all DMS nanomaterials, because of their higher physical, magnetic, magneto-optical and electrical properties which are very much attractive in laser devices, nonlinear optical devices, electroluminescent, photoluminescent, quantum and spintronics devices [3–5]. Transition metal ions like Mn, Fe, Ni Co, Cr etc. are important impurities because of their property to introduce deep trap levels in band gap regions. Transition metal ions play an important role to tune optical, electrical and room temperature magnetic properties of the semiconductors [5]. ZnS is chemically stable semiconductor among all II–VI semiconductors due to its unique physical, optical and electrical properties caused by quantum confinement effect, luminescence efficiency and good host for transition metal ion [3, 6]. Transition metal doped ZnS DMS is good agent for applications in silicon technology [7]. We are highly motivated to Ni, due to its ferromagnetic nature, good conductor of heat, electricity and also its corrosion resistant [3]. Numerous researchers have been investigating the room temperature ferromagnetic properties of transition metals doped ZnS DMS and observing Curie temperature as well as blocking temperature higher than room temperature [3, 8, 9]. Poornaprakash et al. [3], synthesized Ni doped ZnS nanoparticles by refluxing method and investigated dopant induced room temperature ferromagnetism which was

✉ J. P. Borah
  dipraj.saikia7@gmail.com

1   Department of Physics, National Institute of Technology Nagaland, Chumukedima, Dimapur, Nagaland 797103, India

attributed to the long range Ni^{2+}–Ni^{2+} interaction mediated by conduction electrons. Kaur et al. [10], synthesized Cr doped ZnS nanoparticles and observed room temperature ferromagnetism in undoped ZnS nanoparticles which was attributed to the surface defects due to the higher surface to volume ratio of the nanoparticles. They observed ferromagnetic contribution while doped with Cr and reported that the observed room temperature ferromagnetism is the result of the exchange interaction between the localized 'd' spins of the Cr ions and the free delocalized carriers. The unexpected ferromagnetism in DMS arises due to two interacting subsystems; firstly, the delocalized conduction electrons and holes in the valance band, secondly, the localized moment in the transition metal ions. The exchange interaction between the s shell spins of conduction electrons (p shell spins of holes) near band edges and the d shell spins of the transition metal ions results the room temperature ferromagnetism in the diluted system.

In this work, we report the structural, optical and room temperature magnetic properties of pure and Ni doped ZnS nanoparticles. Our basic aim is to analyze the magnetic behavior shown by undoped ZnS nanoparticles and enhanced ferromagnetic behavior after doping of Ni ions in ZnS lattice. We examine the influence of surface defects and interaction mechanisms on the structural, optical and magnetic properties of the undoped and Ni doped ZnS nanoparticles.

2 Experimental analysis

2.1 Synthesis

Undoped and Ni doped ZnS nanoparticles with varying Ni concentration are synthesized by microwave assisted co-precipitation technique [9]. All the chemicals are taken AR grade and are used without purification. For the preparation of undoped ZnS nanoparticles, we dissolved 0.2 M Zinc acetate $[Zn(CH_3COO)_3 \cdot 2H_2O]$ in 50 ml de-ionized water and after stirring for ½ h with magnetic stirrer, we add 0.2 M sodium sulphide $[Na_2S]$ solution prepared in 50 ml de-ionized water drop wise to the above solution. Then the resultant solution is stirred continuously for 3 h till white precipitates are obtained. After getting the precipitates, the precipitates are washed several times by de-ionized water and heat continuously at 90 °C for 8 h to obtain the powder form. For the preparation of Ni doped ZnS nanoparticles for 1, 3 and 5% Ni concentrations, we mixed 0.2 M zinc acetate $[Zn(CH_3COO)_3 \cdot 2H_2O]$ solution prepared in 50 ml de-ionized water, with 0.002 M (for 1%), 0.006 M (for 3%) and 0.01 M (for 5%) nickel chloride $[NiCl_2]$ solution, prepared in 50 ml de-ionized water. The solution is then stirred for 1 h, and after complete mixing we add 0.2 M Na_2S

solution prepared in 50 ml de-ionized water, drop wise to the above solution. The resultant solution is stirred continuously at 80 °C for 3 h until the precipitates are obtained. After obtaining the precipitates, we wash them several times by de-ionized water and heat at 90 °C for 8 h and finally we get powder nanoparticles.

2.2 Characterization

XRD spectra of all the samples are taken by Rigaku Ultima IV X-ray diffractometer operating at 40 KV-40 mA using CuK_α radiation. The elemental analyses (EDAX) are taken using LEO 1430 VP attached with scanning electron microscope (SEM). UV–visible spectra of nanoparticles are carried out by UV–visible spectrometer (SHIMADZU Model: UV-2450) Photoluminescence (PL) spectra of the samples were recorded by fluorescence spectrometer (Cary Eclipse MY15360004). Particle size and morphology is examined by Transmission electron microscope (TECNAI G2 20 S-TWIN (200 KV)). Fourier transform infrared spectroscopy (FTIR) measurements are done by IMPACT 410 FTIR. Raman Analysis is done by Laser Micro Raman System (Horiba Jobin Vyon, Model: LabRam HR). Magnetic properties are recorded by Vibrating Sample Magnetometer (VSM) (Model: 7410 series).

3 Results and discussion

3.1 Structural analysis

The typical XRD spectra of undoped and Ni doped ZnS nanoparticles for different Ni concentrations are illustrated in Fig. 1. All three diffraction peaks corresponding to the lattice planes (111), (220) and (311), which are in agreement with the standard ICDD (DB card No. 00-005-0566) data confirming Cubic Zinc blende structure. No characteristic peaks for secondary phases like Ni, Zn, NiS etc. are detected in the samples, confirming the solubility of the Ni ions in the ZnS host lattice [9, 11]. The diffraction peaks seem to be broadening, which indicates the nanocrystalline nature of the samples [12]. The average crystalline size of the nanoparticles is estimated using Debye Scherrer [9] formula given by

$$D = \frac{k\lambda}{\beta \cos\theta} \tag{1}$$

where, D is the average crystalline size, k is constant (=0.9), β is FWHM and λ is the wavelength of X-ray. It is also observed that the width of the peaks decreases with increasing Ni concentration, which is an indication of increased crystalline size with increasing Ni concentration.
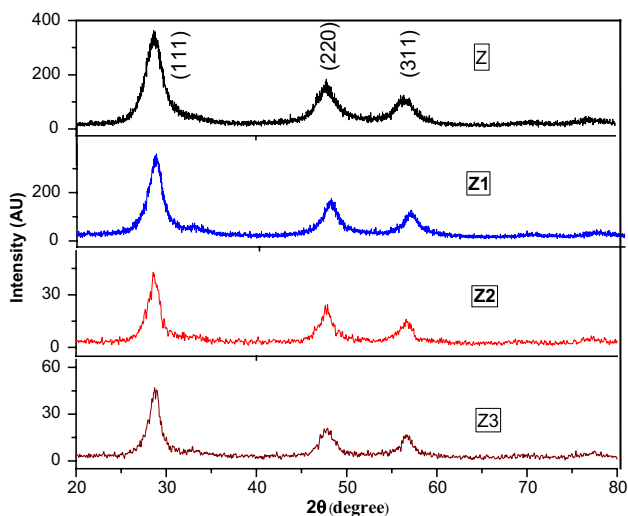
Fig. 1 XRD spectra of undoped (Z) and 1% (Z1), 3% (Z2) and 5% (Z3) Ni doped ZnS nanoparticles. (Color figure online)

The average crystalline sizes for undoped and Ni doped ZnS nanoparticles are found to be in the range of 3–6 nm. The intensity of the XRD peaks is also observed to be decrease with increasing Ni concentration, which is an evidence of reduced crystallinity of the nanoparticles [11, 13]. Kumar et al. [14] reported decreasing trend of the XRD peak intensity with increasing doping concentration in chemically synthesized Fe doped ZnS nanoparticles which indicate the deterioration of the structural quality of ZnS with Fe doping. Similar kind of result was also observed

by Goktas et al. [15] in Mn doped ZnS nanocrystalline thin films synthesized by sol–gel process. They explained that the reduction of crystalline quality of the samples is might be due to the lattice disorder and the strain induced by the vacancies or the substitution of the Mn^{2+} ions in the place of Zn^{2+}.

To extract the structural information, all the XRD patterns of the nanoparticles are analyzed by Rietveld refinement technique [16] by considering $F\bar{4}3$ m space group (Fig. 2). The observed XRD spectra (dotted line) and the calculated spectra (solid line) are indicated by the upper part of the diagram and the difference between the observed and calculated intensities are indicated in the lower part of the diagram. The refined profile parameters, crystalline size and the lattice constants as calculated by rietveld refinement are tabulated in Table 1. The value of the goodness of fit (GOF) for all the samples is found to be very small, which is an indication of the good profile fitting of the structural parameters. The crystalline sizes of undoped and the Ni doped ZnS nanoparticles as obtained from the refinement are found to be in the range of 3–6 nm. The obtained values of the lattice parameters are 5.41, 5.39, 5.38 and 5.36 Å for undoped, 1, 3 and 5% Ni doped ZnS nanoparticles respectively (Table 1). The decrease of lattice constant with increasing Ni concentration is attributed to the compressive strain induced due to the substitution of Ni^{2+} (0.69 Å) in the place of Zn^{2+} (0.78 Å) [11, 17, 18]. The difference in the ionic radii may be distort the structure of the lattice which may lead to the shrinkage of lattice parameter [12, 17].
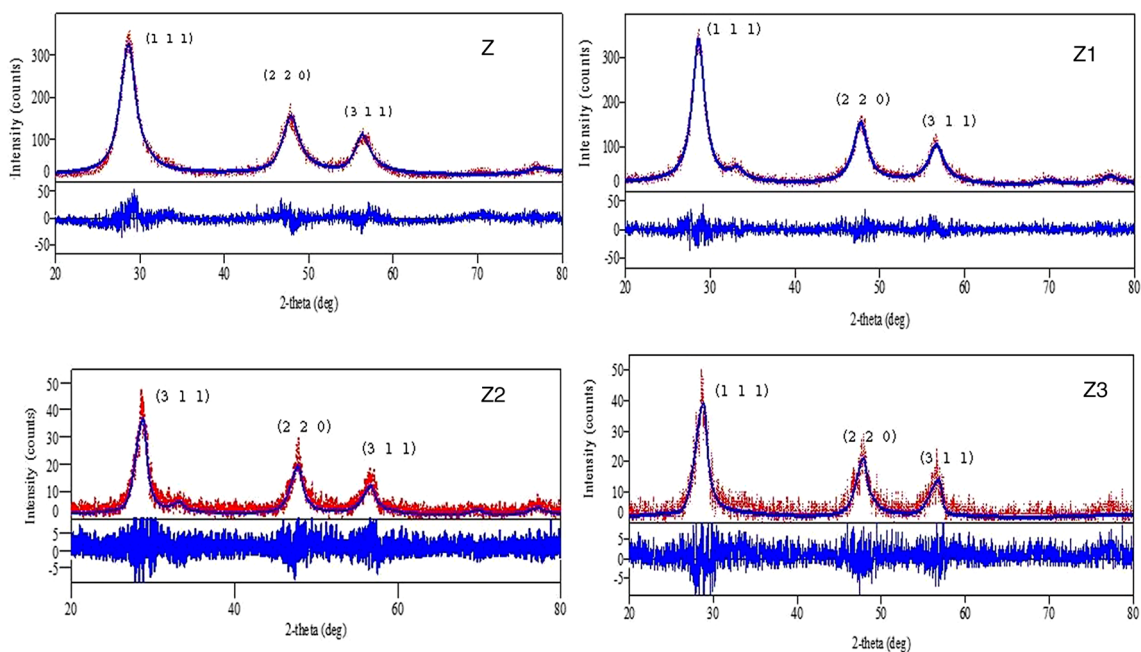

Fig. 2 Rietveld refinement of XRD patterns for undoped (Z), 1% (Z1), 3% (Z2) and 5% (Z3) Ni doped ZnS nanoparticles

Table 1 Refined structural parameters of the undoped and Ni doped ZnS nanoparticles

Sample and Z	Sample p, Z=4	Sample b, Z=4	Sample c, Z=4	Sample d, Z=4
Space group	F$\bar{4}$3 m	F$\bar{4}$3 m	F$\bar{4}$3 m	F$\bar{4}$3 m
Lattice parameters (Å)	5.41	5.39	5.38	5.36
Wavelength (Å)	1.5406	1.5406	1.5406	1.5406
2θ scan range (°)	20–80	20–80	20–80	20–80
2θ scan step (°)	0.02	0.02	0.02	0.02
Volume (Å^3)	157.66	155.79	154.08	153.76
R_p (%)	13.83	13.27	13.90	14.10
R_{wp} (%)	18.87	19.06	20.46	20.1
R_{exp} (%)	16.12	14.69	14.82	14.7
χ^2	1.37	1.68	1.91	1.83
GOF index	1.17	1.29	1.38	1.36
Crystalline size (nm)	3.2	4.5	4.9	5.4

Figure 3 shows the TEM images of undoped (Z) and 3% Ni doped (Z2) ZnS nanoparticles. The representative selected area electron diffraction (SAED) patterns of the samples are shown in the insets of Fig. Z(a) and Fig. Z2(a) which demonstrates the three concentric rings corresponding to (111), (220) and (311) planes of cubic Zinc blende structure. TEM images also reveal that the morphology of the nanoparticles is nearly spherical in shape. The average particle size found to be in the range of 4–7 nm which is well consistence with the XRD results.

From the fig Z2(a), it is also observed that the particles are agglomerated due to the small sized particles and also due to the higher surface energy [1, 11]. The d-spacing from the most prominent lattice plane is evaluated as 3.06 and 2.98 Å for undoped and 3% Ni doped ZnS nanoparticles respectively. The shrinkage of the lattice spacing of the Ni doped ZnS nanoparticles compared to the undoped one is an indication of the incorporation of Ni^{2+} in the Zn^{2+} position [17, 18].

Fig. 3 TEM micrographs of undoped [Z(a) and Z(b)] and 3% Ni doped [Z2(a) and Z2(b)] ZnS nanopartciles
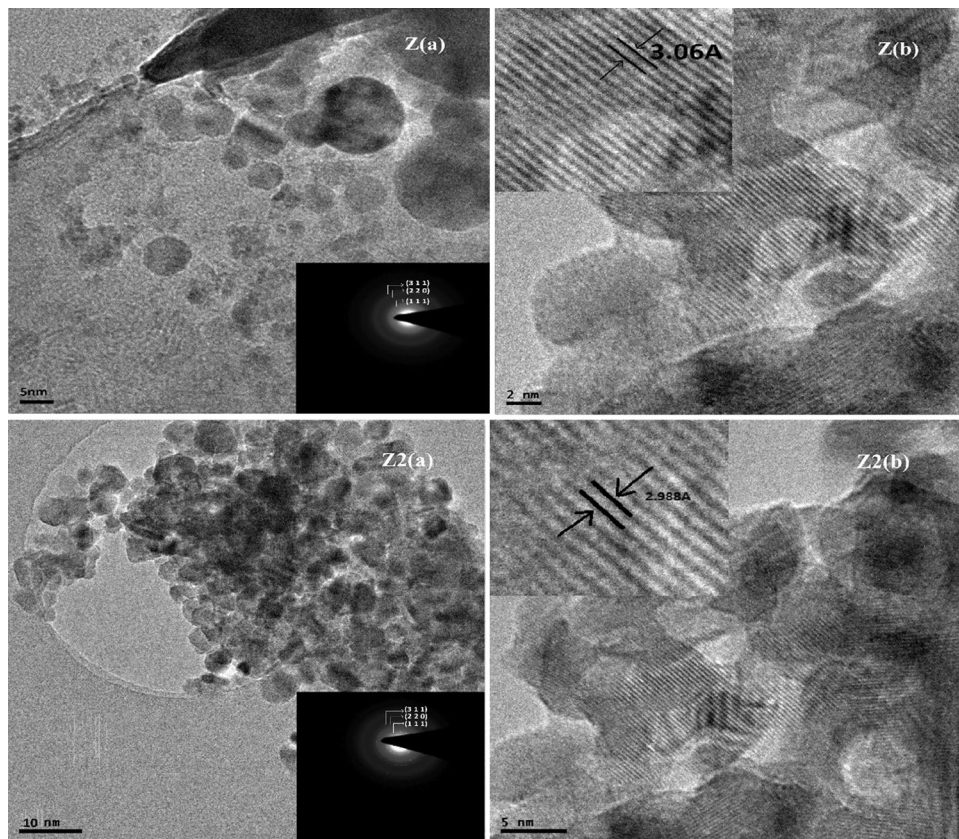
3.2 Elemental analysis

Figure 4 depicts the EDAX spectra of undoped and 1% Ni doped ZnS nanoparticles. It is seen that the spectra contains only the peaks corresponding to Zn, S and O in undoped sample. On the other hand, for Ni doped sample the spectra shows the presence of Zn, S, O and Ni without any other impurities.

3.3 Optical study

3.3.1 UV–visible study

Optical absorption spectra of doped ZnS nanoparticle with different concentrations of Ni, exhibit excitonic absorption features as demonstrated in Fig. 5. The distinct absorption peaks appear at 305, 309 and 315 nm corresponds to 1, 3 and 5% Ni doped ZnS nanoparticles respectively. From the Fig. 5, it is seen that the absorption edge of the samples is red shifted with increasing dopant concentration. This may be accountable to the strong sp–d exchange interaction between the ZnS band electrons and localized d spins associated with the Ni^{2+} ion [19]. We evaluate the band gap of the samples by plotting $(\alpha h\upsilon)^2$ versus photon energy $(h\upsilon)$ and extrapolating the linear portion of the graph to $\alpha = 0$, as illustrated in Fig. 6. Here α is absorption coefficient, h is Planck's constant and υ is the incident photon frequency [6]. The estimated band gap of 1, 3 and 5% Ni doped ZnS nanoparticles are found to be 4.06, 4.01 and
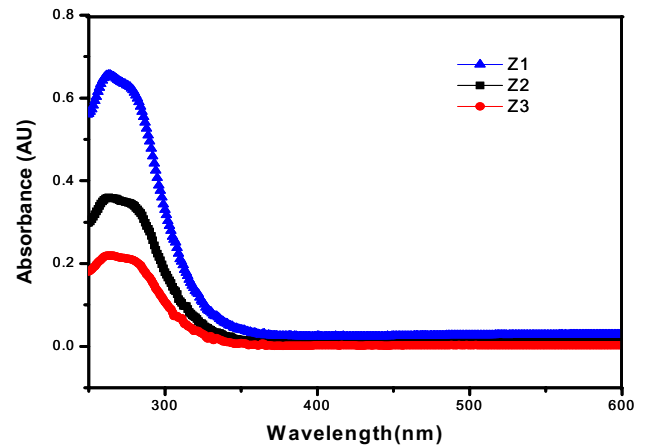

Fig. 5 Absorption spectra of 1% (Z1), 3% (Z2) and 5% (Z3) Ni doped ZnS nanoparticles

3.93 eV respectively. The higher band gap of the doped ZnS compared to the bulk ZnS (3.68 eV) is attributed to the quantum size effect [20, 21]. The decreasing trend of the band gap is an indication of the increased particle size with increasing Ni concentration. The size of the nanoparticles is estimated by the effective mass approximation theory [6] in which the radius of the nanocrystals is related to quantum confinement energy by the relation.

$$\Delta E = \left(\frac{h^2}{8R^2} \right) \left(\frac{1}{m_e^*} + \frac{1}{m_h^*} \right) - \frac{1.8e^2}{4\pi \in R} \tag{2}$$

where, $\Delta E = E_g^{NC} - E_g^B$, [$E_g^{NC}$ and E_g^B are the band gap of nano and bulk semiconductors respectively].

m_e^* and m_h^* are the effective masses of electrons and holes respectively, e is the electronic charge, ϵ is the dielectric constant od the bulk semiconductor, h is the Planck's constant and R is the radius of the nanocrystal. Substituting
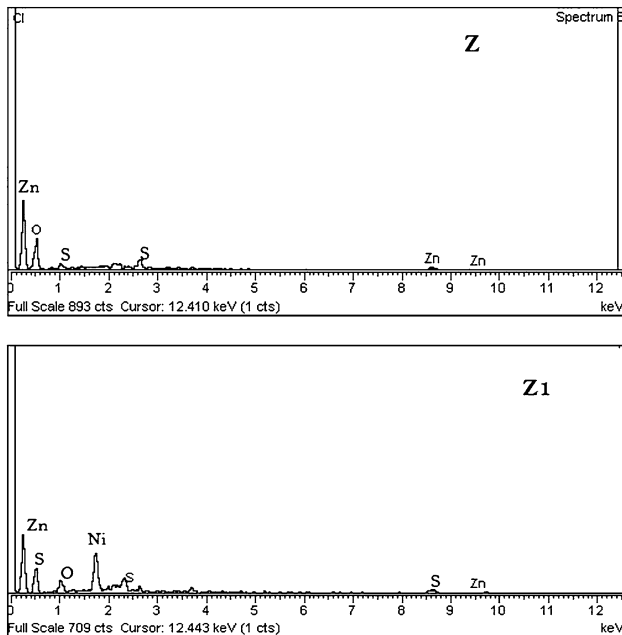

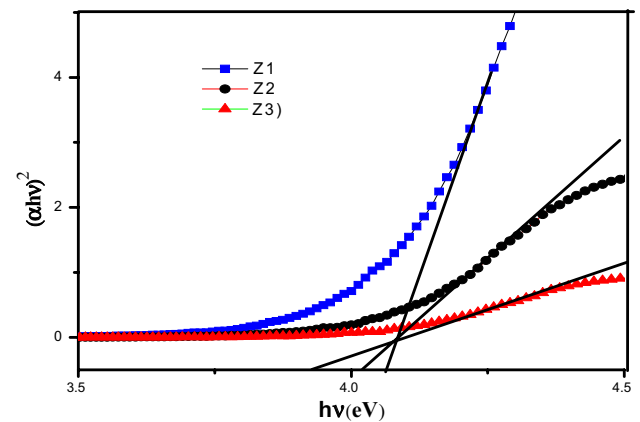**Fig. 4** EDAX spectra of undoped (Z) and 1% (Z1) Ni doped ZnS nanoparticles

Fig. 6 Tauc plot for 1% (Z1), 3% (Z2) and 5% (Z3) Ni doped ZnS

the values of the all the defined parameters in the Eq. (2) for cubic ZnS crysytal, we get the estimated size of 1, 3 and 5% Ni doped ZnS nanoparticles as 4.2, 4.7 and 5.1 nm respectively which are supported with the values obtained from XRD and TEM.

3.3.2 Photoluminescence study

Figure 7 illustrates the room temperature photoluminescence spectra of undoped and Ni doped ZnS nanoparticles recorded with an excitation wavelength of 300 nm. All the samples exhibit two emission peaks centered at ~361 and ~390 nm. The first peak is the characteristic band edge emission of ZnS nanocrystal. On the other hand, the peak centered at ~390 nm is due to the recombination and trapping of hole in the valance band to the electrons in the conduction band through defect states (Zn or S vacancy) of ZnS [11, 22, 23]. The blue emission peak is observed at ~422 nm for undoped and Ni doped ZnS nanoparticles. Similar results have also been reported by Borse et al. [24]. The blue emission is attributed to the sulfur vacancy due to the recombination of the electrons from the shallow states to the Sulfur vacancies (Vs^{2-}) near the valance band [12, 25, 26]. The blue-green emission peak detected at ~484 nm is a sign of Ni in ZnS. This is might be due to the Zn vacancies in the ZnS lattice [27, 28]. In case of cubic $ZnS:Ni^{2+}$ nanocrystals, due to anisotropic hybridization, the lowest multiplet term ^3F of Ni^{2+} ion splits into $^3T_2$, $^3T_1$ and $^3A_2$ states as demonstrated in Fig. 8 and hence luminescence center is formed in ZnS nanoparticles which is related to d–d optical transition of Ni^{2+} ions [29, 30].

So it can be confirmed that, the observed green emission in case of Ni doped ZnS nanoparticles is due to the $^3T_2$–$^3A_2$ transition of Ni^{2+} ion which is replaced by Zn^{2+} ions in
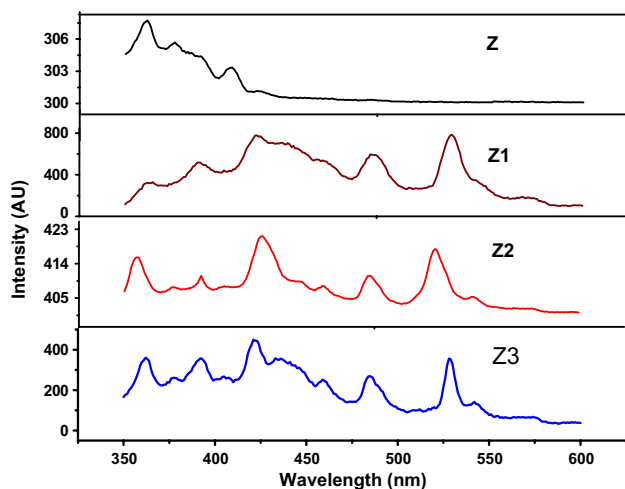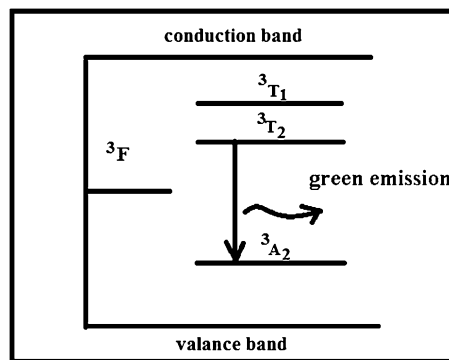

Fig. 8 Energy splitting of Ni^{2+} ion

ZnS lattice [3, 6]. Peng et al. [28] also observed green emission in the range 510–530 nm in Ni and Cu doped ZnS nanoparticles. They speculated that the observed emission arises due to the recombination between the shallow donor level (S vacancy) and the t_2 level of the transition metal ion (Ni^{2+} and Cu^{2+}). Again, it is obvious from the Fig. 7 that the blue emission peak of undoped ZnS nanoparticles is red shifted compared to the Ni doped ZnS nanoparticles which may be due to the quantum confinement effect [6]. The relative intensity of the overall PL emission in doped ZnS nanoparticles decreases with increasing Ni concentration. The decrease of the luminescence intensity with Ni concentration may be due to concentration quenching [11, 20]. The PL quenching with increasing Ni concentration is due to the non-radiative energy transfer from one Ni^{2+} ion to another Ni^{2+} ion [29, 31] at the time of exchange interaction between the nearest neighbors Ni^{2+} ions. This argument is also supported by our magnetic results.

3.4 FT-IR analysis

Figure 9 shows the FT-IR spectra of undoped and Ni doped ZnS nanoparticles for different Ni concentrations are recorded in the range of $4000-400$ cm^{-1}. The peaks observed at ~460 and ~670 cm^{-1} are the characteristics stretching vibrations of cubic ZnS [9, 32]. Moreover, the peak at ~997 cm^{-1} is due to the existence of resonance interaction between vibrational modes of sulfide ions. The broad absorption peak observed at ~3400 m^{-1} is due to the −OH vibration modes which specify the trace amounts of adsorbed water in the nanoparticles surface [6, 11]. The peak observed at ~2380 cm^{-1} for all the samples is due to the C-H stretching vibrations of the alkyl group [23, 33]. This peak may also be due to the C=O stretching modes which arises from the CO_2 absorption on the surface of the nanoparticles [32]. The peaks observed at ~1113 cm^{-1} and ~640 cm^{-1} are assigned to the Zn-OH stretching and bending modes of $Zn(OH_2)$ respectively [6]. Similar peaks at
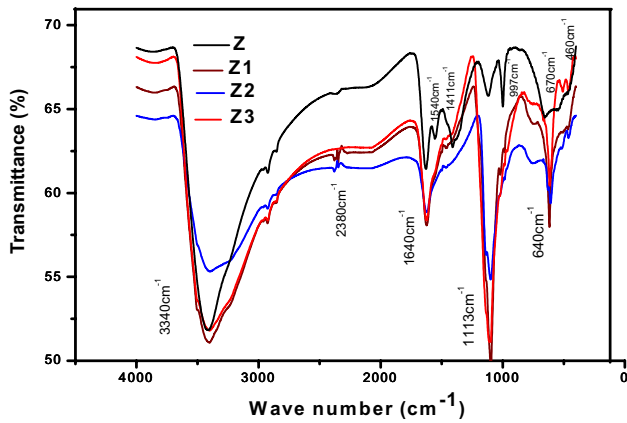

Fig. 7 Photoluminescence spectra of undoped (Z), 1% (Z1), 3% (Z2) and 5% (Z3) Ni doped ZnS nanoparticles

Fig. 9 FTIR spectra of undoped (Z), 1% (Z1), 3% (Z2) and 5% (Z3) Ni doped ZnS nanoparticles. (Color figure online)

were detected at ~618 cm^{-1} and ~1110 cm^{-1} by G. Murugadoss et al. [29] which are due to the formation of microstructure in the prepared samples. The peak at ~1540 cm^{-1} corresponds to the carbonyl (C=O) group in undoped ZnS nanoparticles is shifted to ~1640 cm^{-1} in case of Ni doped ZnS nanoparticles, which clarifies the presence of Ni ions in ZnS lattice. As seen in the Fig. 9, the absorption peaks at ~1113 cm^{-1} and ~640 cm^{-1} are stronger in case of Ni doped ZnS compared to the pure ZnS nanoparticles, which is also an evidence of incorporation of Ni ions in the ZnS host [32].

3.5 Raman analysis

Raman analysis is an important technique to investigate the lattice disorders, crystal defects and incorporation of dopants in the host lattice [34]. Figure 10 depicts the room temperature raman spectra of undoped and 1 and 3% Ni doped ZnS (Z1 and Z2) nanoparticles. For undoped ZnS nanoparticles, Gaussian curve fitting results five peaks at 90, 146, 251, 337 and 441 cm^{-1}. The peaks at 251, 337 cm^{-1} are corresponding to the transverse optical (TO) and longitudinal optical (LO) phonon modes of cubic ZnS respectively [26]. The peaks at 90 and 146 cm^{-1} is assigned to the E$_2$ phonon mode and second order transverse acoustic phonon mode (2TA) [35]. The peak observed at 441 cm^{-1} is due to the LO+LA phonon mode [36, 37]. Schneider et al. [38] and Nelson et al. [39] measured the room temperature raman spectra of cubic ZnS nanoparticles and observed the raman shift near 350 and 270 cm^{-1} which they speculated as the LO and TO phonon modes respectively. In case of Ni doped ZnS nanoparticles, four peaks are found by applying Gaussian curve fitting near 157, 217 and 473 cm^{-1}. The peak at 86 cm^{-1} is assigned to the E$_2$ phonon mode which is also observed in case of undoped ZnS nanoparticles. The peaks at 157 cm^{-1} and
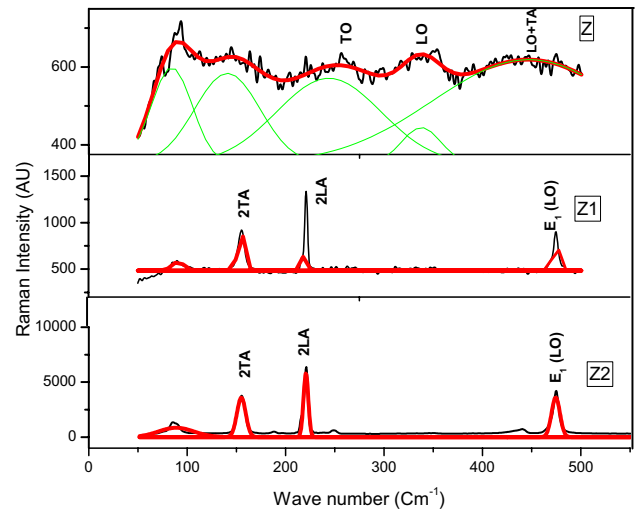

Fig. 10 Raman spectra of undoped (Z), 1% (Z1) and 3% (Z2) Ni doped ZnS, nanoparticles. (Color figure online)

217 cm^{-1} for both the samples b and c are attributed to the second order transverse acoustic phonon (2TA) and second order longitudinal acoustic phonon (2LA) in ZnS respectively [36, 40]. The additional strong band at 473 cm^{-1} is assigned to the E$_1$(LO) mode and also attributed to the S or Zn vacancies of the crystal [34].

3.6 Magnetic analysis

Figure 11 illustrates the variation of magnetization of undoped and Ni doped ZnS nanoparticles with respect
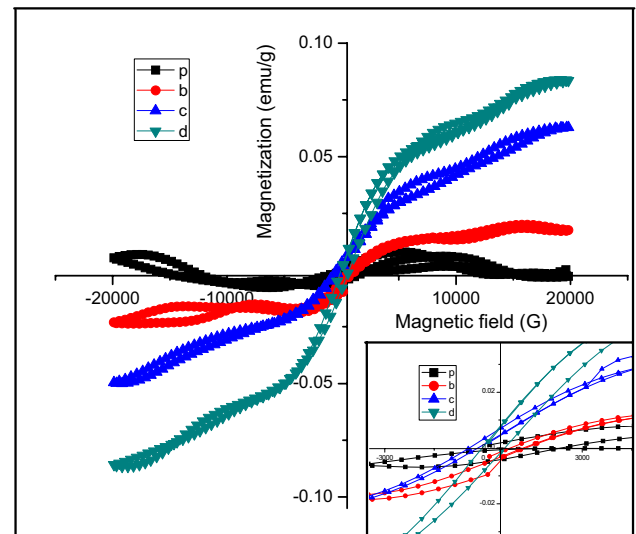

Fig. 11 M-H curves of undoped (Z), 1% (Z1), 3% (Z2) and 5% (Z3) Ni doped ZnS nanoparticles and the *inset* shows the M-H curves in the lower field regions

to applied magnetic field at room temperature. The M-H curves depict that undoped ZnS exhibits magnetic behavior with a weak ferromagnetic contribution whereas Ni doped ZnS nanoparticles exhibits ferromagnetic nature at room temperature. The inset of the Fig. 11 shows the M-H curves of the samples in the lower magnetic field regions which demonstrates the weak ferromagnetic nature of the samples. Our finding is similar as Sunil Kumar et al. [25] where, they observed a mixed behavior of diamagnetic and ferromagnetic in undoped ZnS. Zhaolong Yang et al. [41] also reported room temperature ferromagnetism in undoped CdS nanostructure and concluded that the sulfur vacancy taking an integral part to create room temperature magnetism in semiconductor. Wen-Zhi Xiao et al. [7] investigated the magnetism in undoped ZnS nanoparticles using density functional theory. Generally, Zn atom is surrounded tetragonaly by four S atoms. They reported that, in ZnS crystal, when a Zn vacancy is formed, the sp^3 orbitals of four S atoms surrounding the Zn vacancy tetrahadraly, combined into singlet and triplet states. The magnetic moment arises due to high spin configurations through these singlet and triplet states. They concluded that the ferromagnetism in undoped ZnS nanoparticles is due to the long range coupling mediated by the moments which is induced by Zn vacancy. We also observed a similar kind of behavior. The PL spectrum of undoped sample clearly indicates the presence of sulfur vacancy. So, we believe that the presence of vacancy promote the ferromagnetism in undoped ZnS nanoparticle. Moreover, due to the higher surface area of nanoparticles, uncompensated surface spins are dominating in the nanoparticles compared to the bulk which leads to surface defects and results a net magnetization [42]. Figure 11 (Z1-Z3) shows the room temperature magnetic hysteresis (M-H) loop for the 1%, 3% and 5% Ni doped ZnS nanoparticles respectively. All the three samples show the distinct ferromagnetic behavior. The variation of the coercivity, retentivity and saturation magnetization is tabulated in the Table 2. To understand the origin of room temperature magnetism in case of transition metal doped semiconductors have emerged as the most controversial and challenging field of today's Nanomagnetism research. The

origin of room temperature ferromagnetism in case of these materials are thought to be causes of some phenomenon, like induce of transition metal ions in the cations in the host lattice [43], direct exchange interaction between the transition metal ions [7, 30], exchange interactions between localized spins of transition metal ion and free delocalized carriers (sp-d) [38, 44], presence of intrinsic defects [42] etc. Recently, S. Kumar et al. [26] observed room temperature ferromagnetism in Ni doped ZnS nanoparticles, due to the substitution of Ni^{2+} ions into the ZnS host lattice in the place of Zn^{2+}. They explained the ferromagnetic ordering at lower concentration of Ni, whereas, with increasing Ni concentration, the nanoparticles show a nonsaturated M-H curve because of antiferromagnetic ordering due to reduced Ni–Ni distance in the ZnS lattice. D. Amaranatha Reddy et al. [9], also achieved room temperature ferromagnetism in Cr doped ZnS nanoparticles and reported that the observed ferromagnetic is dopant induced and originated from the exchange interaction between the 'd' spins of the Cr ions through delocalized carriers. The ferromagnetic nature in our study is not due to the presence any clusters of Ni or any other secondary phases like NiS, Ni^{2+}, Zn^{2+} etc. (which is confirmed from XRD study) but due to the exchange coupling between the localized Ni^{2+} ions mediated by the delocalized carriers present in the nanoparticles [16, 26]. As shown in Fig. 11, at lower concentration of Ni, the ferromagnetic nature is clearly pronounced with a saturated M-H curve (Z1). The surface related phenomena are responsible for the pronounced ferromagnetic nature in case of the lower doped sample. In relatively small nanoparticles, the exchange interaction energy between the neighboring small magnetic dipoles presented in the surface, affects the nearest neighbors to be aligned in the same direction. The population of the magnetic dipoles aligned in the same direction is increased at the surface due to high surface to volume ratio of the nanoparticles, which promotes the nanoparticles to be more ferromagnetically ordered state [26, 45]. In our previous studies of Fe in similar system (ZnS) [11], it was realized that; at the higher concentration of Fe (10%), the short range antiferromagnetic coupling between the Fe–Fe ions suppresses the ferromagnetic nature of the nanoparticles. The M-H curves of the samples Z2 and Z3 are not fully saturated, which is an indication of the presence of antiferromagnetic coupling between Ni–Ni ions at higher doping concentrations [26, 46]. Thus we can conclude that in the present samples the ferromagnetic ordering is lost beyond 1% Ni doping concentration.

4 Conclusion

In conclusion, undoped and Ni doped ZnS nanoparticles with different Ni concentrations are successfully prepared

Table 2 Coercivity, Remanent magnetization and saturation magnetization values of undoped (Z), 1% (Z1), 3% (Z2) and 5% () Ni doped ZnS nanoparticles

Sample	Coercivity (G)	Remanent magnetization (M_s) (emu/g)	Saturation magnetization (M_r) (emu/g)
Z	107	0.57×10^{-3}	0.78×10^{-2}
Z1	160	2.01×10^{-3}	1.4×10^{-2}
Z2	123	1.21×10^{-3}	2.6×10^{-2}
Z3	182	1.73×10^{-3}	4.5×10^{-2}

by microwave assisted co-precipitation technique. XRD and TEM results confirm the cubic Zinc blend structure with an average crystalline size in the range of 3–7 nm. Refinement of the structural parameters shows a good profile fitting and the values of the parameters are consistence with the experimental results. UV–visible spectra show the enhancement of band gap in Ni doped ZnS nanoparticles compared to the bulk ZnS, which is the result of quantum confinement effect. Photoluminescence spectra depicts the vacancy related emission spectra attributed to the $^3T_2$-$^3A_2$ transition of Ni^{2+} ion in Ni doped ZnS nanoparticles also shows the concentration quenching effect at higher doping. Room temperature magnetic studies reveal the weak ferromagnetism behavior in undoped ZnS nanoparticles due to surface vacancy states. Ni doped ZnS nanopartcles show room temperature ferromagnetic behavior which is the result of exchange interaction between the localized d electrons of the Ni^{2+} ions with free delocalized carriers.

References

1. N. Eryong, L. Donglai, Z. Yunsen, B. Xue, Y. Liang, J. Yong, J. Zhifeng, S. Xiaosong, App. Surf. Sci. **257**, 8762 (2011)
2. S.A. Wolf, D.D. Awschalom, R.A. Buhrman, J.M. Daughton, S.V. Molnar, M.L. Roukes, A.Y. Chtchelkanova, D.M. Treger, Science. **294**, 1488 (2001)
3. B. Poornaprakash, S. Sambasivam, D.A. Reddy, G. Murali, R.P. Vijayalakshmi, B. K. Reddy, Ceram. Int. 40, 2677–2684 (2014)
4. M. Shamsipur, H. R. Rajabi and O. Khani, Mat. Sci. Semcon. Proc. 16, 1154 (2013)
5. A. Mandal, A. Dandapat, G. De, Analyst **137**, 765 (2012)
6. R. Sahraei, S. Darafarin, J. Lumin. **149**, 170–175 (2014)
7. W.Z. Xiao, L.L. Wang, Q.Y. Rong, G. Xiao, B. Meng, J. Appl. Phys. **115**, 213905 (2014)
8. S. Sambasivam, D.P. Joseph, J.G. Lin, C. Venkateswaran, J. Solid State Chem. **182**, 2598–2601 (2009)
9. D.A. Reddy, G. Murali, R.P. Vijayalakshmi, B.K. Reddy, Appl. Phys. A 105, 119–124 (2011)
10. P. Kaur, S. Kumar, A. Singh, C.L. Chen, C.L. Dong, T.S. Chan, K.P. Lee, C. Srivastava, S.M. Rao, M.K. Wu, Superlattices Microstruct., 83, 785–795 (2015)
11. D. Saikia, R.D. Raland, J.P. Borah, Phys. E, 83, 56–63 (2016)
12. P.C. Patel, S. Ghosh, P.C. Srivastava, J. Mater. Sci. **50**, 7919–7929 (2015)
13. Y. Li, C. Cao, Z. Chen, Chem. Phys. Lett. **517**, 55 (2011)
14. S. Kumar, N.K. Verma, J Mater Sci: Mater Electron **26**, 2754–2759 (2015)
15. A. Goktas, I.H. Mutlu, J. Sol-Gel Sci. Technol. **69**, 120–129 (2014)
16. N.G. Imam, M.B. Mohamed, Superlattices Microstruct. 73, 203–213 (2014)
17. W. Cheng, X. Ma, J. Phys. Conf. Ser. **152**, 012039-1-012039-6 (2009)
18. M. Molaei, F. Karimimaskon, A. Lotfiani, M. Samadpour, H. Liu, J. Lumin. **143**, 649–652 (2013)
19. J. Kaur, M. Sharma, O.P. Pandey, Opt. Mater. **47**, 7–17 (2015)
20. Z. Rui, L. Yingbo, S. Shuqing, Opt. Mater. **34**, 1788–1794 (2012)
21. D.A. Reddy, A. Diviya, G. Murali, R.P. Vijayalakshmi, B.K. Reddy, Phys. B **406**, 1944–1949 (2011)
22. Y. Liu, Z. Li, W. Zhong, L. Zhang, W. Chen, Q. Li, Nanoscale Res. Lett. **9**, 389 (2014)
23. D. Saikia, J.P. Borah, M. Jangra, A. Puzari, Indian J. Phys. **90**, 549–555 (2016)
24. P.H. Borse, N. Deshmukh, R.F. Shinde, S.K. Date, S.K. Kulkarni, J. Mater. Sci. **34**, 6087–6093 (1999)
25. S. Kumar, N.K. Verma, J. Mater. Sci. **25**, 1132–1137 (2014)
26. S. Kumar, C.L. Chen, C.L. Dong, Y.K. Ho, J.F. Lee, T.S. Chan, R. Thangavel, T.K. Chen, B.H. Mok, S.M. Rao, M.K. Wu, J. Alloy Compd. **554**, 357–362 (2013)
27. N. Karar, F. Singh, B.R. Mehta, J. Appl. Phys. **95**, 656–660 (2004)
28. W.Q. Peng, G.W. Cong, S.C. Qu, Z.G. Wang, Opt. Mater. **29**, 313–317 (2006)
29. G. Murugadoss, M.R. Kumar, Appl. Nanosci. 4, 67–75 (2014)
30. P. Yang, M.K. Lhu, D. Xu, D. Yuan, J. Chang, G.J. Zhou, M. Pan, Appl. Phys. A 74, 257 (2002)
31. Q. Pan, D. Yang, Y. Zhao, Z. Ma, G. Dong, J. Qiu, J. Alloys Compd. **579**, 300–304 (2013)
32. R.M. Ibrahim, M. Markom, H. Abdullahc, ECS J. Solid State Sci. Technol. 4, R31–R37 (2015)
33. M. Abdelaziz, E.M. Abdelrazek, Phys. B 390, 1 (2007)
34. B. Pal, D. Sarkar, P.K. Giri, Appl. Surf. Sci. **356**, 804–811 (2015)
35. M. Abdulkbadar, B. Thomas, Nanostruct. Mater. 5, 289–298 (1995)
36. J.H. Kim, H. Rho, J. Kim, Y.J. Choi, J.G. Park, J. Raman Spectrosc. **43**, 906–910 (2012)
37. Q. Xiong, J. Wang, O. Reese, L.C.L.Y. Voon, P.C. Eklund, Nano. Lett. 4, 1991 (2004)
38. J. Schneider, R.D. Kirby, Phys. Rev. B **6**, 1290–1294 (1972)
39. W.G. Nilsen, Phys. Rev. B **182**, 838–850 (1969)
40. Y.T. Nien, I.G. Chen, Appl. Phys. Lett. **89**, 261906 (2006)
41. Z. Yang, D. Gao, Z. Zhu, J. Zhang, Z. Shi, Z. Zhang, D. Xue, Nanoscale Res. Lett. **8**, 17 (2013)
42. P. Elavarthi, A.A. Kumar, G. Murali, D.A. Reddy, J. Alloys Compd. **656**, 510–517 (2016)
43. K.R. Gunasekhar, S. Kumar, N.K. Verma, J. Supercond. Nov. Magn. 28, 137–142 (2015)
44. H. Bi, S. Li, Y. Zang, Y. Du, J. Magn. Magn. Mater. 277, 363–367 (2004)
45. P.K. Sharma, R.K. Dutta, A.C. Pandey, J. Colloid interface Sci. **345**, 149 (2010)
46. P.K. Sharma, R.K. Dutta, A.C. Pandey, S. Layek, H.C. Verma, J. Magn. Magn. Mater. 321, 2587 (2009)